Observing the in situ chiral modification of Ni nanoparticles using scanning transmission X-ray microspectroscopy

Watson, D. J., Acharya, S., Nicklin, R. E. J. and Held, G. (2014) Observing the in situ chiral modification of Ni nanoparticles using scanning transmission X-ray microspectroscopy. Surface Science, 629. pp. 108-113. ISSN 0039-6028 doi: https://doi.org/10.1016/j.susc.2014.03.018 Available at http://centaur.reading.ac.uk/37853/

Surface Science 629 (2014) 108–113

Contents lists available at ScienceDirect

Surface Science

journal homepage: www.elsevier.com/locate/susc

Observing the *in situ* chiral modification of Ni nanoparticles using scanning transmission X-ray microspectroscopy

David J. Watson [a,*], Sushma Acharya [a], Richard E.J. Nicklin [b], Georg Held [b]

[a] Department of Chemistry, University of Surrey, Stag Hill, Guildford GU2 7XH, UK
[b] Department of Chemistry, University of Reading, Whiteknights, Reading RG6 6AD, UK

ARTICLE INFO

Available online 24 March 2014

Keywords:
Heterogeneous catalysis
STXM
Enantioselective hydrogenation
Chiral modifier

ABSTRACT

Enantioselective heterogeneous hydrogenation of C═O bonds is of great potential importance in the synthesis of chirally pure products for the pharmaceutical and fine chemical industries. One of the most widely studied examples of such a reaction is the hydrogenation of β-ketoesters and β-diketoesters over Ni-based catalysts in the presence of a chiral modifier. Here we use scanning transmission X-ray microscopy combined with near-edge X-ray absorption fine structure spectroscopy (STXM/NEXAFS) to investigate the adsorption of the chiral modifier, namely (R,R)-tartaric acid, onto individual nickel nanoparticles. The C K-edge spectra strongly suggest that tartaric acid deposited onto the nanoparticle surfaces from aqueous solutions undergoes a keto-enol tautomerisation. Furthermore, we are able to interrogate the Ni $L_{2,3}$-edge resonances of individual metal nanoparticles which, combined with X-ray diffraction (XRD) patterns showed them to consist of a pure nickel phase rather than the more thermodynamically stable bulk nickel oxide. Importantly, there appears to be no "particle size effect" on the adsorption mode of the tartaric acid in the particle size range ~90–~300 nm.

1. Introduction

Chemical routes to enantio-enriched, and ultimately enantio-pure, compounds have attracted great interest in the past decades, stimulating remarkable progress in homogeneous enantioselective catalysis. The culmination of this was the award of the Nobel Prize in Chemistry in 2001 to Noyori, Sharpless and Knowles for their inputs in advancing homogeneous asymmetric hydrogenations and oxidations [1,2]. In contrast to the numerous examples of enantioselective homogeneous catalysts reported in the literature the number of successful heterogeneous systems is small — despite the numerous advantages of heterogeneous systems over their homogeneous counterparts. Various strategies have been pursued to design heterogeneous enantioselective catalysts that combine high catalytic activity with suitable stereochemical control of the reaction, the most successful of which include the modification of the catalytic metal surface by a strongly adsorbing chiral compound, the modifier [3–5]. The progress in heterogeneous enantioselective catalysis is reflected by the rapidly growing number of scientific publications and a number of recent reviews of the subject [4,6–10]. The importance of chirally modified metals in asymmetric synthesis has also stimulated a number of surface science studies aimed at understanding the fundamental properties of the adsorption of chiral molecules at catalytically relevant surfaces. These studies usually combine model surfaces, *i.e.* single crystals, with 'ideal' adsorption conditions, *i.e.* ultra-high vacuum [11–13]. There are relatively few studies published, with the notable exception of the work of Jones and Baddeley [14] who studied the adsorption of tartaric acid from solution under a number of different conditions, that utilise 'real' catalytic materials and/or conditions — this is something we address in this paper.

To date the heterogeneous catalytic systems that have undergone the most interrogation include the enantioselective hydrogenation of α-ketoesters over Pt-based catalysts [3,15–17] and the enantioselective hydrogenation of β-ketoesters and β-diketoesters over Ni-based catalysts [4,18–20].

These enantioselective surface reactions are controlled by the presence of an adsorbed chiral molecule on the surface of the active metal. In the case of the Ni/β-ketoester system, (R,R)-tartaric acid (R,R-TA) or amino acids, such as alanine and aspartic acid [21,22], are used as the chiral modifier and an enantiomeric excess [23] of R-methyl-3-hydroxybutyrate (R-MHB) is observed following the hydrogenation of methylacetoacetate (MAA) (Fig. 1).

The precise pathway of the reaction and the mechanism of this enantioselective control have, however, not been yet verified; though several models of the modified surface have been proposed to explain the activity [3,24–26]. One possible explanation being a two-point hydrogen-bonding (H-bonding) model in which the protons of the hydroxyl groups of the tartaric acid H-bond to the β-ketoester or β-diketone oxygen atoms. This arrangement sterically favours the

* Corresponding author. Tel.: +44 1483 686836.
E-mail address: d.j.watson@surrey.ac.uk (D.J. Watson).

http://dx.doi.org/10.1016/j.susc.2014.03.018
0039-6028/

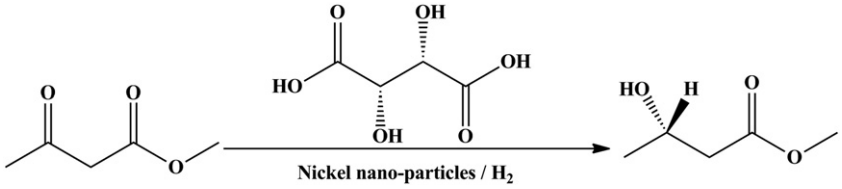

Fig. 1. Schematic diagram of the β-ketoester hydrogenation reaction showing a typical reactant, methylacetoacetate, the major product, (R)-methyl-3-hydroxybutyrate ((R)-MHB) and the chiral modifier, (R,R)-tartaric acid. When (S,S)-tartaric acid is substituted as the chiral modifier the major product is the S-enantiomer, (S)-MHB.

adsorption of one β-ketoester conformer over the other, thus resulting in enantioselective hydrogenation (Fig. 2) [24–26]. Satisfyingly, this model also explains both of the diastereoisomers formed in the chiral dehydrogenation of acetylacetonate [27]. Furthermore it accounts for the hydrogenation of prochiral ketones containing sterically hindered alkyl groups, which can form only one hydrogen bond, with the net result being a very striking reversal of enantioselectivity. In Fig. 2, it is clear that hydrogenation of MAA in this conformation would result in the R-form of MHB being formed. An alternative proposed model involves the formation of 2-dimensional chiral co-crystalline domains on the metal surface formed by the propensity of the chiral adsorbate molecules to self-assemble into ordered structures [4]. This template surface model is a reasonable one when used in relation to extended surfaces (for example single crystals or the larger nanoparticles used in this study) but may reach limitations on very small nanoparticles due to limited terrace widths. There have been many attempts to further understand the active site in TA-Ni catalysts for the hydrogenation of MAA but no clear explanation of the catalytic phenomena has been proposed which would bring this into light [4,25–27].

In this paper we aim to collect detailed *in situ* photoabsorption spectra of species involved in the topical enantioselective hydrogenation reaction of methylacetoacetate. We will use the excellent spatial resolution afforded by the PolLux scanning transmission X-ray microspectroscopy (STXM) beamline of the Swiss Light Source to locate individual nanoparticles and subsequently measure the Ni $L_{2,3}$-edge NEXAFS spectra as well as the C K-edge NEXAFS spectra of the adsorbed tartaric acid molecules.

There are numerous articles in the literature where STXM has been used to study polymer systems [29–31], carbon nanotubes [32,33] and clays [34,35] but, to our knowledge, none that examine the adsorption of chiral modifier molecules (or any other small organic molecule) onto catalytically relevant metal nanoparticles. Here we report, for the first time observed using STXM, the adsorption of tartaric acid onto Ni nanoparticles; an investigation that will contribute to the understanding of the mechanism of this important and topical enantioselective heterogeneous hydrogenation reaction.

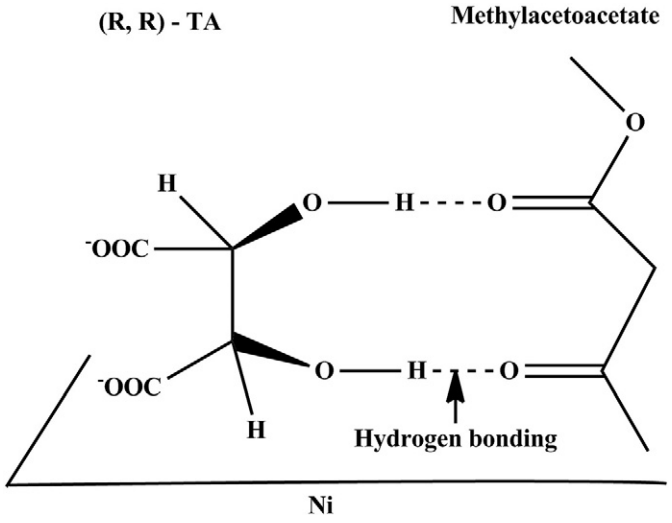

Fig. 2. Schematic representation of one of the models for the mechanism of the interaction between (R,R)-tartaric acid adsorbed at the catalyst surface and methylacetoacetate. Adapted from reference [28].

2. Materials and methodology

Nickel chloride (anhydrous) (98%), hydrazine ($N_2H_4.H_2O$) (98%), sodium-hydroxide (≥99%), methyl 2-hydroxyethyl cellulose (98%), (R,R)-tartaric acid (99%) and methyl acetoacetate (99%) were all purchased from Sigma-Aldrich (UK) and were used without further purification.

2.1. Nanoparticle synthesis

Ni nanoparticles were prepared by adding methyl 2-hydroxyethyl cellulose (0.2 wt.%) to 1.2 M aqueous $NiCl_2$ solution at 90 °C. NaOH solution (20 wt.%) was added drop-wise until a pH of 11 was achieved. From this point two different procedures were carried out depending on the intended use of the resulting nanoparticles. A) For Ni catalysts to be used for XRD analysis and high-pressure hydrogenation reactions: 6.2 M $N_2H_4.H_2O$ was added directly to the solution either with or without simultaneous addition of sufficient α-Al_2O_3 to result in a 10% metal loading. B) For Ni catalysts to be used for STXM analysis: Prior to the addition of the 6.2 M $N_2H_4.H_2O$ (the reduction step) silicon nitride windows were immersed into the reaction mixture until the reduction of the metal salt was complete. Two types of window were used: either 'clean' Si_3N_4 window (Silson Ltd, UK) or Si_3N_4 windows that had previously been modified with 10 nm of alumina applied from an aluminium evaporator source located in a vacuum system with an O_2 partial pressure of ~1×10^{-6} mbar. The alumina coated windows were further heated in air for 12 h to ensure that the aluminium was fully oxidised and also to relieve lattice strain that could damage the membrane, the 'clean' windows were used without further treatment. Finally, the product was washed with distilled water and ethanol several times to remove impurities, and then dried at room temperature.

2.2. Nanoparticle modification with tartaric acid

Tartaric acid was adsorbed onto the samples, when required, from aqueous solution. A single droplet of 0.5 M (R,R)-tartaric acid (pH = 1.8, T = 298 K) was placed onto the sample window. The solution was allowed to sit for 3 min and then the window was washed three times in clean Milli-Q water before drying prior to insertion into the vacuum chamber.

2.3. Powder X-ray diffraction

The phases present in the products were identified from their powder X-ray diffraction (PXRD) patterns, which were collected on a Bruker D8 diffractometer using Ni filtered Cu Kα radiation (λ = 1.540598 Å) operated at a voltage of 40 kV and a current of 30 mV. The measurements were carried out with a step scan mode: step size = 0.02 (degrees 2θ), time per step = 18.87 s, in the range of 50–140 degrees 2θ. The goniometer was calibrated with a cubic α-quartz standard (a_h = 5.4309 Å). Corrections for systematic deviation in 2θ were applied.

2.4. X-ray microspectroscopy

NEXAFS microspectroscopy was performed at the PolLux beamline at the Swiss Light Source, Paul Scherrer Institut, Villigen, Switzerland [36,37]. The PolLux microscope operates in a transmission geometry with a zone plate (outer zone width of 35 nm) used to focus monochromatic X-rays from the beamline (bending magnet beamline with monochromator and higher order suppressor [38]) onto the sample. Samples were mounted in the sample chamber, which was evacuated to ~10^{-6} mbar using a turbo pump. The sample is rastered with respect to the focused X-ray beam using an interferometer-controlled piezo stage. The transmitted X-ray intensity through the sample was recorded using a scintillator and photomultiplier tube and measured as a function of energy (dependent on the material being examined, with a resolution of 0.1 eV) and position (with resolution better than 40 nm). An order sorting aperture (OSA) is used to block zero order light that is not diffracted by the zone plate and orders higher than the first order. Full NEXAFS spectra were taken over selected linear regions of the sample with as short a dwell time as practicable to minimize radiation damage. All NEXAFS spectra presented were acquired in transmission mode and are therefore bulk averaged. In each case an individual baseline of an area of the same sample not containing a nanoparticle was acquired simultaneously to allow correction for beam intensity. STXM images were acquired at either 854.5 eV (nickel) or 285 eV (carbon) for maximum contrast.

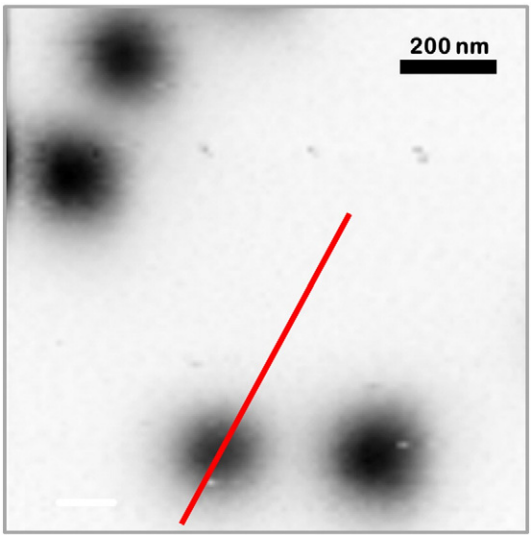

Fig. 4. Scanning transmission X-ray microspectroscopy image of Ni nanoparticles. Image size = 1 × 1 μm, photon energy = 850 eV, step size = 10 nm. Red line indicates typical line profile (line length = 1 μm) used for NEXAFS acquisition and covers both nanoparticle and background region used for normalization.

3. Results and discussion

XRD was used to confirm the formation of pure Ni (rather than the more thermodynamically favourable NiO) nanoparticles without the need for further calcination/reduction steps. Fig. 3 compares the XRD pattern of the produced Ni nanoparticles with that of commercially available Ni powder (<100 nm) between 5 and 110 degrees 2θ. In both samples one can observe characteristic peaks at 44.5, 51.8, 76.4, 92.9 and 98.3 degrees 2θ indicating the presence of pure nickel (111), (200), (220), (311) and (222) phases, respectively, although the ratios show small differences. Peak broadening observed in the XRD patterns is indicative of a reduction of particle size [39,40]. With the presence of pure nickel nanoparticles confirmed, samples were prepared as described in the Materials and methodology section to be examined using STXM.

A representative 1 × 1 μm STXM image of Ni nanoparticles deposited on a clean Si_3N_4 window at a photon energy of 854.5 eV is shown in Fig. 4. The image shows four nanoparticles of ~90–140 nm in diameter.

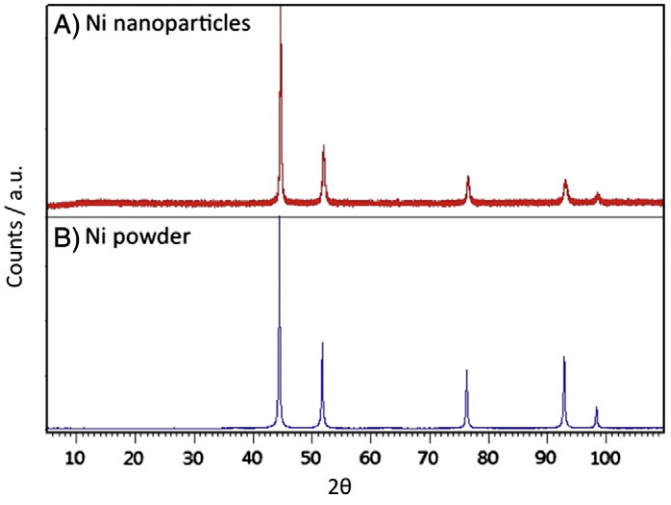

Fig. 3. X-ray diffractogram of: (A) Ni nanoparticles used in study, and (B) commercially available Ni powder with a nominal size of <100 nm. Peak positions and FWHM values of the two samples are comparable suggesting that the composition and mean particle sizes were similar.

The exact size of the nanoparticles could only be determined within the resolution limits of the Fresnel zone plate (35 nm). This zone plate was chosen to reduce the photon flux impinging on small areas of the sample during longer data acquisitions to avoid beam damage. The red line shown in Fig. 4 indicates the trajectory of a typical line scan used for NEXAFS acquisition. When selecting a line profile over which to scan one should note that it should include data collected from the nanoparticle and, importantly, also from the background of the sample. Information from the background of the sample was used to normalize the spectra for variations in X-ray beam intensity with photon energy and time. The accuracy of the positioning system in the STXM endstation on the PolLux beamline and also the distinct spatial configuration of groups of nanoparticles meant that it was possible to return to the same individual nanoparticle several times — even after the sample plate had been removed from the analysis chamber and replaced at a later time. This allowed us to examine exactly the same nanoparticle under a number of different conditions and also to compare distinctly different nanoparticles under the same conditions, the results of which are now shown and discussed in detail.

Fig. 5 shows normalized Ni $L_{2,3}$-edge NEXAFS from three different nanoparticles (i–iii) and also, for comparison, from Raney Nickel (iv). The three nanoparticles chosen covered a range of sizes from ~90 nm (i) to ~170 nm (ii) and finally a larger nanoparticle of ~300 nm (iii) to allow us to conduct a particle size effect study. Raney Nickel typically consists of very large (tens of micrometres) but porous particles [41,42]. The porosity of the particles is a result of the aluminium (which can contribute up to 50% of the mass of the catalyst when manufactured) being leached from the solid in either a 'pre-modification' stage or under reaction conditions [43,44]. Due to the fact that the STXM experiment is conducted in a transmission mode, the typical larger Raney Nickel particles could not be studied. Instead a crystallite of ~500 × 900 nm was chosen. This was deemed large enough to share the same bulk properties as the several micrometre size particles. The dominant features of all the spectra shown in Fig. 5 are the resonances at 853–854 eV and ~871 eV. These correspond to the Ni L_3 and L_2 adsorption edges, respectively. For all but the smallest of the nanoparticles the maxima of the L_3 adsorption edge fall at 853.3 eV, in the case of the 90 nm particle (spectrum (i)) the maximum is shifted to higher photon energies by ~0.4 eV. There is also a marked difference in the shape of the 853.3 eV peak for the largest of the nanoparticles (iii) and the Raney Nickel sample (iv) with an apparent high

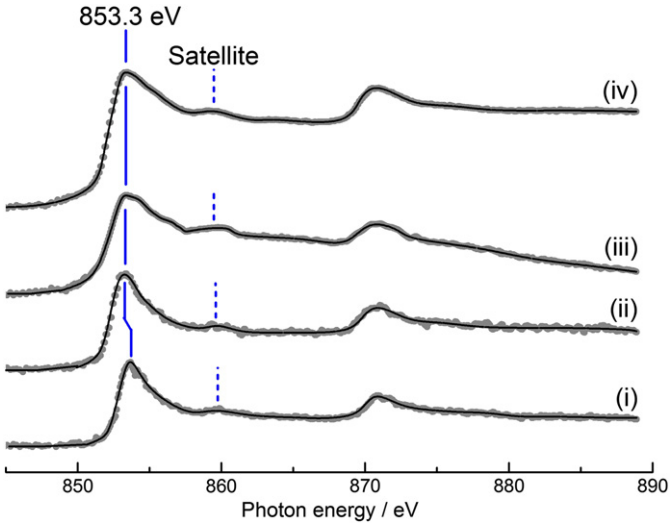

Fig. 5. Ni $L_{2,3}$-edge NEXAFS from: (i) ~90 nm Ni particle; (ii) ~170 nm Ni particle; (iii) ~300 nm Ni particle; and (iv) ~500 nm Raney Nickel particle.

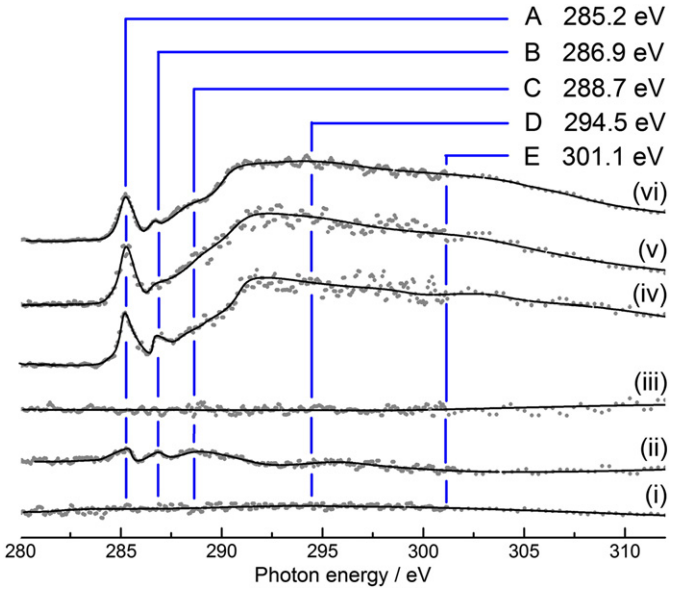

Fig. 6. C K-edge NEXAFS of: (i) 'as produced' Ni nanoparticle showing lack of surface contamination; (ii) tartaric acid adsorbed onto a clean Si_3N_4 window; (iii) tartaric acid adsorbed onto a Ni nanoparticle deposited onto an alumina coated Si_3N_4 window; tartaric acid adsorbed onto ~90 nm (iv), ~170 nm (v) and ~300 nm (vi) Ni nanoparticles deposited onto a clean Si_3N_4 window.

photon energy shoulder appearing at ~856 eV. Both the position and the shape of the L_3-edge of 3*d* metals are strongly reliant on the empty 3*d* and 4*sp* states [45,46]. The full width–half maximum (FWHM) of the nickel L_3 adsorption edge for the pure, bulk metal is 2.3 eV. Senkovskiy et al. found that a $Ni_{50}Ti_{50}$ had a FWHM of 2.7 eV and that the L_3 adsorption edge was also shifted by 0.7 eV (from 852.7 eV to 853.4 eV) [47]. These findings correlate very well to our current work where the L_3 adsorption edge for untreated Raney Nickel (nominally a $Ni_{1-x}Al_x$ where $0.1 \leq x \leq 0.5$) was found to be 853.3 eV. This resonance also appears to have a larger FWHM than any of the corresponding 'pure' metal nanoparticles.

We postulate that the shift to higher photon energy of the L_3 adsorption edge as seen in spectrum (i) for the ~90 nm particle is a result of the greater contribution to the particle of the surface oxide layer formed under ambient conditions. It is not unlikely that a Ni catalyst would be exposed to air unintentionally, even for the shortest period, before it is modified for use in a catalytic reaction. As such, this spectra may be of additional importance. The fact that a small shift is observed in the L_3- and L_2-edges but that the spectra retains all of the characteristics of the 'clean' nickel nanoparticles suggests that it would still perform as desired catalytically. Indeed, Jones and Baddeley studied the adsorption of (R,R)-tartaric acid on oxidised Ni(111) surfaces using a combination of RAIRS and TPD and found that the thermal stability of the adsorbed layer was actually enhanced on the oxidised surface. Furthermore they suggested that oxidised surfaces can facilitate etching from the surface to expose a chiral array of Ni which may be capable of catalytic enantioselectivity without the need for additional chiral modifiers [48]. The concept of enantioselective etching was first introduced by Attard et al. regarding the Pt-catalysed hydrogenation of methyl pyruvate [14]. Additionally, as will be shown and discussed later, oxidation of the nickel surface appears to have no effect on the state in which the tartaric acid adsorbs.

Along with the features described in detail above, all spectra show the expected separation between the L_3 and L_2 adsorption edges of ~17.2 eV and also a corresponding high photon energy satellite resonance [49] — although this is less prominent for the L_2 adsorption edge.

Fig. 6 shows C K-edge NEXAFS taken under different conditions either before (i) or after (ii)–(vi) the adsorption of (R,R)-tartaric acid. Notwithstanding spectra (i) and (iii) the spectra all show resonances instantly recognizable as originating from small organic molecules containing multiple order bonds. A summary of the assignments and associated transitions is given in Table 1.

Fig. 6(i)–(iii) can be considered as 'control' samples, the results of which put the later results into context. Fig. 6(i) shows NEXAFS spectra of a nickel nanoparticle before the adsorption of any additional species. It can be used in conjunction with the XRD pattern to confirm that the nanoparticles were not only pure nickel, but also had clean surfaces that were not contaminated with a cellulose residue from the synthesis procedure (we cannot exclude the presence of a surface oxide layer, though). This is an important but often overlooked detail when synthesizing nanoparticles that will be used for catalysis — the nature and cleanliness of the surface are paramount.

Fig. 6 (ii) represents the results of C K-edge NEXAFS after the adsorption of tartaric acid from aqueous solution and subsequent washing onto a completely clean (as received) Si_3N_4 window. For a molecule such as tartaric acid which does not contain C═C bonding one would not normally expect to see C 1s → π* resonances as low as 285 eV. C═O resonances are typically only found in the range 286–288 eV [52,53], whereas, peaks in the range 284–286 eV are typically indicative of C═C bonding [50,51]. However, Fig. 6 (ii) shows a weak signal with resonances at 285.2 eV and 286.9 eV and several smaller, ill-defined, features between ~289 and 302 eV. The presence of the 285.2 eV peak suggests that the tartaric acid molecule has undergone a chemical change upon adsorption involving the formation of a C═C double bond. There are two possible explanations for this transformation leading to the appearance of a C 1s → π* resonance. First, a condensation reaction whereby the C═C bond is formed between the two chiral centres leading to the loss of H_2O and ultimate loss of all chirality from the modifier molecule. Second a keto-enol tautomerisation as shown in Fig. 7 which represents an equilibrium between two constitutional isomers, the keto- and enol-forms. In the latter case the chirality of just one of the

Table 1
C K-edge NEXAFS resonance assignments [50–53].

Peak	Energy/eV	Assignment
A	285.2	C 1s → $\pi^*_{(C=C)}$
B	286.9	C 1s → $\pi^*_{(C=O)}$
C	288.7	C 1s → $\sigma^*_{(C-H)}$
D	294.5	C 1s → $\sigma^*_{(C-C)}$
E	301.1	C 1s → $\sigma^*_{(C-O)}$

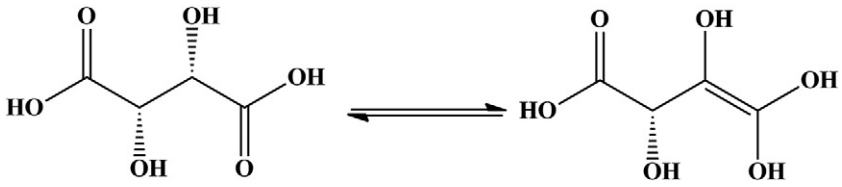

Fig. 7. Keto-enol equilibrium showing the tautomeric forms of tartaric acid.

chiral centres is lost due to sp^2 hybridization. Evidence suggests that this is the more likely explanation as tautomers such as this have been observed previously under similar conditions. Ghoria et al. showed, using STXM, that the keto-enol equilibrium constant of malonic acid (a di-carboxylic acid that is structurally similar to tartaric acid) showed a strong dependence on the relative humidity of the aerosol that deliquesced particles of the organic suspended in [54]. The higher the relative humidity, the greater the amount of the enol form present — they concluded that similar carboxylic acids may also exist in predominantly enol forms. It is perhaps not unusual then that we might observe significant tautomerism in the current study where the tartaric acid being studied was adsorbed onto the surface from an aqueous solution.

Despite the weak signal seen in Fig. 6 (ii) the resonances appear at the expected photon energies (see Table 1 for full assignment of resonances) and suggest that a very small amount of tartaric acid adsorbs, in approximately equal amount of the keto- and enol-forms, on the clean Si_3N_4 window. Importantly, this verifies our use of the background signal obtained from the extended line profile (as described above) to normalize the signal from the nanoparticle, *i.e.* we are able to eliminate any contribution, however small, to the spectra of tartaric acid adsorbed on the clean window. As such we can be confident that the C K-edge adsorptions shown later originate only from interactions with the nanoparticle itself.

Of equal importance is the result of adsorbing tartaric acid onto nickel nanoparticles deposited onto an alumina-coated window (~10 nm thickness Al_2O_3) as shown in Fig. 6 (iii). Subtraction of the background signal from the signal of the nanoparticle itself results in an almost flat and featureless spectrum. This can only be a result of subtracting two almost identical C K-edge NEXAFS signals and indicates that tartaric acid adsorbs onto alumina and the nickel nanoparticle in a similar mode, and to a similar extent. While this may not affect the overall activity of the catalyst it does have important implications when conducting studies to optimize the concentration of modifier (in this case, tartaric acid) to metal surface area ratio.

Finally, we present C K-edge NEXAFS spectra of tartaric acid adsorbed from aqueous solution onto nickel nanoparticles deposited onto clean Si_3N_4 windows. As shown in 6 (ii) there will be very little adsorption onto the clean window and therefore any features observed must originate from molecules adsorbed onto the nanoparticle surface. Spectra 6 (iv)–(vi) are dominated by prominent resonances due to C 1s → π* and C 1s → σ* transitions. All three spectra are very similar and differ only in that they represent adsorption resonances of tartaric acid adsorbed onto different sized particles; namely, the same ~90 nm (iv), ~170 nm (v) and ~300 nm (vi) nanoparticles that were examined in Fig. 5 (i–iii). In contrast to adsorption on the clean window (Fig. 6 (ii)), when adsorbed onto nickel nanoparticles the ratio of the 285.2 eV and 286.9 eV resonances in NEXAFS suggests that the tartaric acid is predominantly in the enol form. The main difference between the three spectra is the improvement in the 'quality' of the data (*i.e.* a reduction in signal-to-noise) that results from the ability to average the signal over a larger number of points when collecting data from larger nanoparticles. Accordingly, we have shown that the adsorption of tartaric acid from aqueous solutions onto the three distinctly different nanoparticles presented here is unaffected by particle size. This is perhaps unsurprising due to the generally large size of the nanoparticles used in the study. If the spatial resolution of the instrument would allow investigation of nanoparticles in the 5–50 nm size range one might expect to see more pronounced differences caused by size effects and reduced terrace widths resulting in disruption of the long-range order of the adsorbed overlayer of chiral modifier molecules.

4. Conclusions

In summary we have shown that it is possible to use the excellent spatial resolution of STXM to interrogate $L_{2,3}$-edge resonances of individual, catalytically relevant, metal nanoparticles. The NEXAFS and XRD showed nanoparticle to consist of a pure nickel phase rather than the more thermodynamically stable bulk nickel oxide. Furthermore, the reproducibility and accuracy of the experiment allowed the same nanoparticles to be located after the sample had been treated under several different conditions. Differences in the shape and position of the L_3-edge resonance could also be used to infer information about the electronic structure and surface state of the material.

It was also possible to observe directly the adsorption of a chiral modifier, namely R,R-tartaric acid, onto a 'real' catalyst sample consisting of nanoparticulate nickel. C K-edge spectra strongly suggest that tartaric acid deposited from aqueous solutions undergoes a transformation on the metal surface akin to an enolisation, evidenced by the presence of strong C1s → π* resonances in the C═C region as well as the expected π* resonances at C═O photon energies. Importantly, there appears to be no "particle size effect" on the adsorption mode of the tartaric acid in the particle size range ~90–~300 nm.

Acknowledgements

The authors acknowledge funding from the EPSRC and the Department of Chemistry, University of Surrey for funding for S. Acharya, (University of Surrey Doctoral Training Grant), and EPSRC for funding for R.E.J. Nicklin (EP/G068593/1).

We are extremely grateful to Benjamin Watts and Jörg Raabe at the Swiss Light Source whose outstanding efforts have made these experiments possible.

Synchrotron experiments conducted at the SLS were supported by the European Commission under the 7th Framework Programme: Research Infrastructures (Grant Agreement Number 226716). The PolLux end station is financed by the German Minister für Bildung und Forschung (BMBF) through contracts 05KS4WE1/6 and 05KS7WE1.

References

[1] W.S. Knowles, Angew. Chem. Int. Ed. 41 (2002) 1998.
[2] R. Noyori, Angew. Chem. Int. Ed. 41 (2002) 2008.
[3] Y. Orito, S. Imai, S. Niwa, J. Chem. Soc. Jap. 8 (1979) 1118.
[4] C. Baddeley, J. Top. Catal. 25 (2003) 17.
[5] D.J. Watson, R.J.B.R.J. Jesudason, S.K. Beaumont, G. Kyriakou, J.W. Burton, R.M. Lambert, J. Am. Chem. Soc. 131 (2009) 14584.
[6] A. Baiker, H.U. Blaser, Handbook of Asymmetric Heterogeneous Catalysis, in: G. Ertl, H. Knozinger, J. Weitkamp (Eds.), vol. 5, 1997, p. 2422.
[7] E. Klabunovskii, G.V. Smith, A. Zsigmond, Heterogeneous Enantioselective Hydrogenation — Theory and Practice, vol. 31Springer, Dordrecht, 2006.
[8] G.J. Hutchings, Annu. Rev. Mater. Res. 35 (2005) 143.
[9] H.U. Blaser, F. Spindler, M. Studer, Appl. Catal. A Gen. 221 (2001) 119.
[10] G. Kyriakou, S. Beaumont, R. Lambert, Langmuir 27 (2011) 9687.
[11] S.M. Barlow, R. Raval, Surf. Sci. Rep. 50 (2003) 201.
[12] C.J. Baddeley, G. Held, Chiral Molecules on Surfaces, Comprehensive; Nanoscience and Technology, Elsevier, Amsterdam, 2010. 105.
[13] T. Eralp, A. Ievin, A. Shavorskiy, S.J. Jenkins, G. Held, J. Am. Chem. Soc. 134 (2012) 9615.

[14] T.E. Jones, C.J. Baddeley, J. Phys. Chem. C 111 (2007) 17558.
[15] T. Mallat, E. Orglmeister, A. Baiker, Chem. Rev. 107 (2007) 4863.
[16] G.A. Attard, J.E. Gillies, C.A. Harris, D.J. Jenkins, P. Johnston, M.A. Price, D.J. Watson, P. B. Wells, Appl. Catal. A Gen. 222 (2001) 393.
[17] B. Minder, T. Mallat, P. Skrabal, A. Baiker, Catal. Lett. 29 (1994) 115.
[18] Y. Izumi, Angew. Chem. Int. Ed. 10 (1971) 871.
[19] Y. Izumi, Adv. Catal. 32 (1983) 215.
[20] M.A. Keane, G. Webb, Chem. Commun. 22 (1991) 1619.
[21] M.A. Keane, Langmuir 13 (1997) 41.
[22] M.A. Keane, Langmuir 10 (1994) 4560.
[23] Enantiomeric excess (e.e.) is calculated as the difference in the amounts of the two chiral product produced divided by the total amount of chiral product produced and is expressed as a percentage. e.e. (%) = ([R-enantiomer] − [S-enantiomer]) / ([R-enantiomer] + [S-enantiomer]) × 100.
[24] T.E. Jones, C.J. Baddeley, Surf. Sci. 519 (2002) 237.
[25] M.O. Lorenzo, S. Haq, T. Bertrams, P. Murray, R. Raval, C.J. Baddeley, J. Phys. Chem. A 103 (1999) 10661.
[26] A. Tai, T. Harada, H. Ozaki, M. Imaida, M. Nakahata, Chem. Soc. Jap. 55 (1982) 2186.
[27] A. Tai, K. Ita, T. Harada, Chem. Soc. Jap. 54 (1981) 223.
[28] K. Ito, T. Harada, A. Tai, Y. Izumi, Chem. Lett. (1979) 1049.
[29] B. Watts, C.R. McNeill, Macromol. Rapid Commun. 31 (2010) 1706.
[30] X. He, B.A. Collins, B. Watts, H. Ade, C.R. McNeill, Small 8 (2012) 1920.
[31] D. Slep, J. Asselta, M.H. Rafailovich, J. Sokolov, D.A. Winesett, A.P. Smith, H. Ade, Y. Strzhemechny, S.A. Schwarz, B.B. Sauer, Langmuir 14 (1998) 4860.
[32] E. Najafi, J. Wang, A.P. Hitchcock, J. Guan, S. Dénommée, B. Simard, J. Am. Chem. Soc. 132 (2010) 9020.
[33] A. Felten, C. Bittencourt, J.-J. Pireaux, M. Reichelt, J. Mayer, J. Hernandez-Cruz, A.P. Hitchcock, Nano Lett. 7 (2007) 2435.
[34] Z. Martin, I. Jimenez, M. Angeles Gomez, H.W. Ade, D.A. Kilcoyne, D. Hernadez-Cruz, J. Phys. Chem. B 113 (2009) 11160.
[35] Z. Martin, I. Jimenez, M.A. Gomez-Fatou, M. West, A.P. Hitchcock, Macromolecules 44 (2011) 2179.
[36] J. Raabe, G. Tzvetkov, U. Flechsig, M. Boge, A. Jaggi, B. Sarafimov, M.G.C. Vernooij, T. Huthwelker, H. Ade, D. Kilcoyne, T. Tyliszczak, R.H. Fink, C. Quitmann, Rev. Sci. Instrum. 79 (2008) 113704.
[37] U. Flechsig, C. Quitmann, J. Raabe, M. Böge, R. Fink, H. Ade, AIP Conf. Proc. 879 (2006) 505.
[38] U. Frommherz, J. Raabe, B. Watts, R. Stefani, U. Ellenberger, AIP Conf. Proc. 1234 (2010) 429.
[39] H. Wang, X. Kou, L. Zhang, J. Li, Mater. Res. Bull. 43 (2008) 3529.
[40] V.D. Mote, Y. Purushotham, B. Dole, J. Theor. Appl. Phys. 6 (2012) 2251.
[41] T.-K. Yang, D.-S. Lee, J. Haas, "Raney Nickel" in Encyclopedia of Reagents for Organic Synthesis, John Wiley, New York, 2005.
[42] M.S. Wainwright, 3.2 skeletal metal catalysts, in: G. Ertl, H. Knözinger, J. Weitkamp (Eds.), Preparation of Solid Catalysts, Wiley-VCH Verlag, Weinheim, Federal Republic of Germany, 1999, p. 28.
[43] T. Osawa, T. Harada, O. Takayasu, Top. Catal. 13 (2000) 155.
[44] P. Kukula, L. Cervený, Appl. Catal. A Gen. 223 (2002) 43.
[45] S. Hüfner, Photoelectron Spectroscopy: Principles and Applications, 3rd ed., Springer, Berlin, Heidelberg, New York, 2003.
[46] J. Stöhr, NEXAFS Spectroscopy, Springer, New York, 1992.
[47] B.V. Senkovskiy, D.Yu. Usachov, A.V. Fedorov, O.Yu. Vilkov, A.V. Shelyakov, V.K. Adamchuk, J. Alloys Compd. 537 (2012) 190.
[48] T.E. Jones, C.J. Baddeley, J. Mol. Catal. A Chem. 216 (2004) 223.
[49] T. Jo, A. Tanaka, J. Electron Spectrosc. 117–118 (2001) 397.
[50] O. Dheza, H. Adea, S.G. Urquhart, J. Electron Spectrosc. 128 (2003) 85.
[51] V.K. Kanuru, G. Kyriakou, S.K. Beaumont, A.C. Papageorgiou, D.J. Watson, R.M. Lambert, J. Am. Chem. Soc. 132 (2010) 8081.
[52] K. Brandt, M.E. Chiu, D.J. Watson, M.S. Tikhov, R.M. Lambert, J. Am. Chem. Soc. 131 (2009) 17286.
[53] S.K. Beaumont, G. Kyriakou, D.J. Watson, O.P.H. Vaughan, A.C. Papageorgiou, R.M. Lambert, J. Phys. Chem. C 114 (2010) 15075.
[54] S. Ghorai, A. Laskin, A.V. Tivanski, J. Phys. Chem. A 115 (2011) 4373.